Extended depth-of-field resolution enhancement microscopy imaging for neutralizing the impact of mineral inhomogeneous surface

Heng Sun,[1,6] Xinran Xu,[1,6] Qianxiong Shi,[2] Junzhang Chen,[1] Darui Jin,[1] Yan Li,[2] Dong Ye,[3] Yong Lai,[2,*] and Xiangzhi Bai[1,4,5,*]

*Correspondence: yonglai@pku.edu.cn (Y. L.); jackybxz@buaa.edu.cn (X. B.)

Received: September 13, 2023; Accepted: June 21, 2024; Published Online: July 1, 2024; https://doi.org/10.59717/j.xinn-geo.2024.100083

GRAPHICAL ABSTRACT

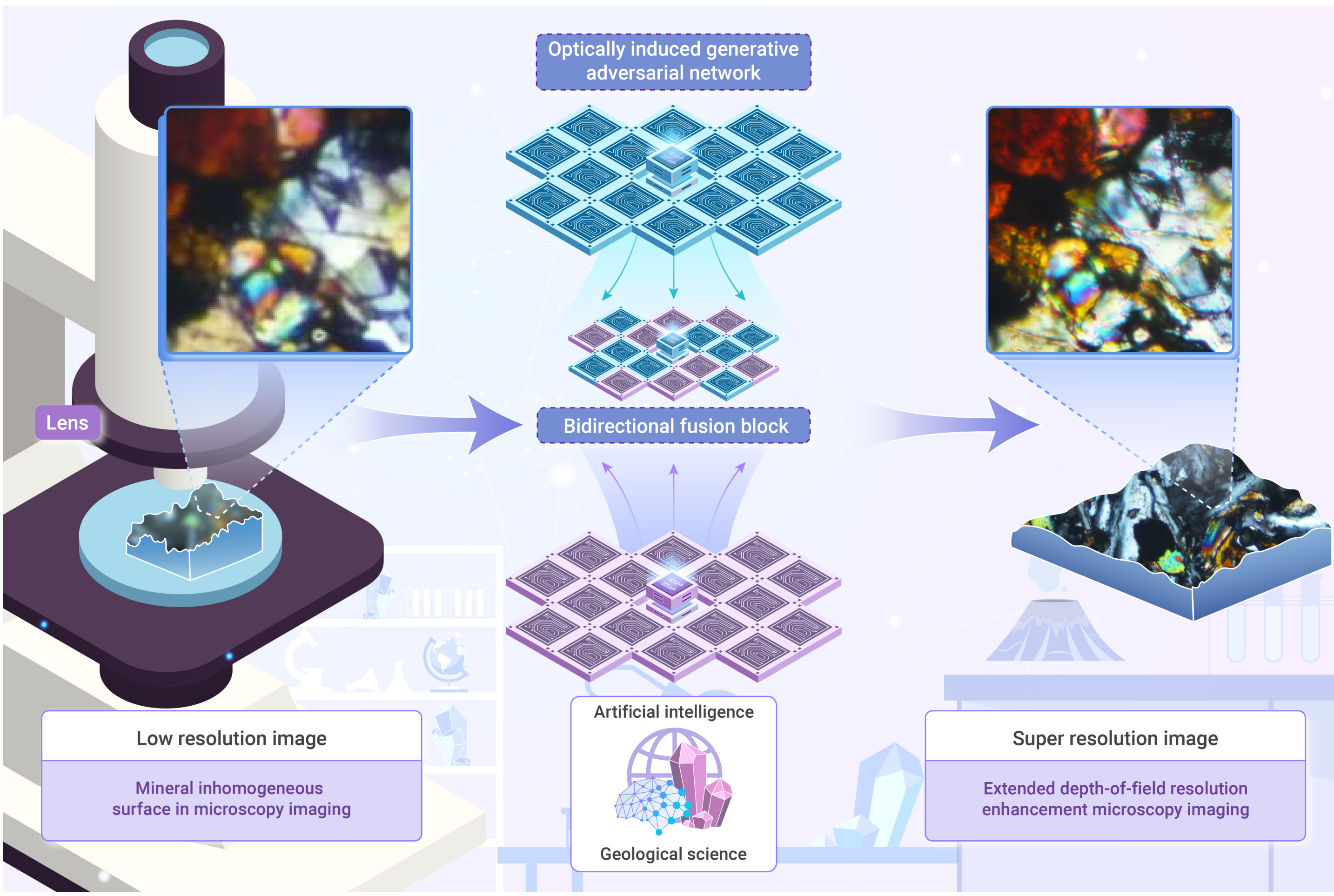

PUBLIC SUMMARY

- Mineral uneven surface aggravates conflict between depth-of-field (DOF) and resolution in microscopy imaging.
- DOF from low-resolution image is revealed as oracles for neutralizing impact of mineral inhomogeneous surface.
- Optically induced generative adversarial network (OIGAN) is proposed by integrating DOF information from minerals.
- OIGAN significantly improves the performance in microthermometry of fluid inclusions and mineral classification.

Extended depth-of-field resolution enhancement microscopy imaging for neutralizing the impact of mineral inhomogeneous surface

Heng Sun,[1,6] Xinran Xu,[1,6] Qianxiong Shi,[2] Junzhang Chen,[1] Darui Jin,[1] Yan Li,[2] Dong Ye,[3] Yong Lai,[2,*] and Xiangzhi Bai[1,4,5,*]

[1]Image Processing Center, Beihang University, Beijing 102206, China

[2]The Key Laboratory of Orogenic Belts and Crustal Evolution, Peking University, Beijing 100871, China

[3]School of Art and Design, Shenzhen Polytechnic University, Shenzhen 518055, China

[4]State Key Laboratory of Virtual Reality Technology and Systems, Beihang University, Beijing 100191, China

[5]Advanced Innovation Center for Biomedical Engineering, Beihang University, Beijing 100083, China

[6]These authors contributed equally

*Correspondence: yonglai@pku.edu.cn (Y. L.); jackybxz@buaa.edu.cn (X. B.)

Received: September 13, 2023; Accepted: June 21, 2024; Published Online: July 1, 2024; https://doi.org/10.59717/j.xinn-geo.2024.100083

Citation: Sun H., Xu X., Shi Q., et al., (2024). Extended depth-of-field resolution enhancement microscopy imaging for neutralizing the impact of mineral inhomogeneous surface. The Innovation Geoscience 2(3): 100083.

One of the most fundamental experimental methods in geoscience is to observe minerals under high magnification objectives. However, uneven microsurfaces in thin sections occur due to the irregular constituent distribution and varying hardness of minerals in natural rocks. Consequently, the conflict between large depth-of-field (DOF) and high-resolution in microscopy imaging leads to random out-of-focus issues when observing thin sections with high resolution microscopy. Although existing super-resolution algorithms promise to improve visual performance, reconstructing images with both large DOF and high-resolution simultaneously remains challenging. We address this problem by guiding the networks with optical information. Utilizing DOF information from low-resolution data, we propose an optically induced generative adversarial network (OIGAN) to neutralize the impact through computational imaging. In OIGAN, optical DOF information from low-resolution data facilitates to achieve spatial-adaptive extended-DOF resolution enhancement imaging, without incorporating extended DOF high-resolution data for supervision. The approach, trained and evaluated on the dataset with 233,156 images (115,346 pairs of low- and high-resolution data), outperforms four comparison methods on various minerals and optical conditions, leading to at least 1.54dB increase on peak signal-to-noise ratio (PSNR). Specifically, OIGAN significantly improves the accuracy of fluid inclusion ice-melting temperature measurement, reducing mean error by 65%, and enhances mineral classification accuracy with 1.5%~15% increase. OIGAN offers an insight of integrating physical knowledge into neural networks, facilitating self-identification of minerals, automatic microthermometry of fluid inclusions and other geoscience tasks via microscopy.

INTRODUCTION

Observing thin sections with an objective lens of more than 50× magnification is a fundamental experimental method in geoscience.[1,2] For example, observing the boundary and Becke lines in thin sections can help infer relative refractive index of minerals. Identifying out fluid inclusions and measuring the ice-melting temperature aid in mineralization analysis. To prepare thin sections, natural rocks are typically polished to around 0.03mm. However, uneven microsurfaces are inevitable in thin sections owing to irregular constituent spatial distribution and varying hardness of minerals. For example, of the three main components in granite, quartz has a hardness of 7, while mica has a hardness of 2~3. Diverse chemical composition and sophisticated changes in the chemical process of minerals also make the surface height variance random and unpredictable. Consequently, observing minerals in rock thin sections requires larger depth-of-field (DOF) comparing with biomedical samples that have even surfaces.

In the applications of mineral microscopy imaging, the ability of extended DOF resolution enhancement imaging is highly desired. However, there is a correlation between the minimum resolution distance Δr and DOF Δd of microscopes (See analysis in Methods of Supplementary Information):

$$\Delta d \propto \Delta r^2, \tag{1}$$

Therefore, the principle of microscopy imaging demonstrates that high magnification and extended DOF are inversely related. The uneven surfaces of thin sections further aggravate the conflict between DOF and resolution in mineral microscopy imaging. When observing thin sections with polarizing microscopes under high magnification objective lens, it is challenging to achieve microscopy imaging with high-resolution and clear focus in full field of view (FOV) simultaneously. Observations with high-resolution microscopes extremely suffer from random out-of-focus issues in FOV. The imaging process is presented in Figure 1A. Numerous important applications, including mineral identification, analysis of metallogenic conditions and microthermometry of fluid inclusion, are notably affected by this issue. Thus, an effective method to mitigate the conflict between large DOF and high-resolution in mineral microscopy imaging is essential to the analysis of microscopic structures and will open up possibilities for geological discoveries.

Numerous attempts have been made to extend either resolution or DOF in microscopy imaging, ranging from hardware implementations to software processing. For resolution enhancement, some super-resolution microscopy technologies have been proposed.[3-7] Nonetheless, these methods usually require special fluorophores, optical modulation, and extensive computation of imaging data, making them time-consuming and limited to specific samples. Image super-resolution algorithms focus on image resolution enhancement using high-resolution data and corresponding synthesized low-resolution data pairs, with substantial efforts devoted to solving degradation between different resolutions.[8-12] For DOF enhancement, some techniques achieve imaging with deeper DOF, such as super-high magnification lens zoom three-dimension microscopes with zoom optical system, which compose the content at different depths by moving specimen stage or objective lens in Z-axis. There are also some methods proposed to acquire extended DOF data in a single shot, such as by wavefront coding, phase masks and so on.[13-15] In these cases, extra prior knowledge and development of imaging systems are necessary, such as point spread function, sophisticated mechanisms and optical setups. Refocusing methods primarily recover defocusing images by estimating degradation, requiring data from different axial locations.[16,17] To summarize, many methods are designed to improve imaging performance in a single aspect, either resolution or DOF. But in mineral microscopy imaging, imaging quality is affected by both resolution and DOF. Hence, a computational imaging method to achieve both resolution and DOF enhancement fast and simultaneously has emerged from practical necessity in mineral microscopy imaging.

Deep learning has spread over diverse fields quickly in recent years and has been used to reconstruct high-quality data in computer vision tasks, such as image inpainting and super-resolution.[18-21] Recently, deep learning methods have also been applied to microscopy imaging in fields such as biology, medicine, geoscience and so on.[22-35] For instance, they have been applied for fluorescence microscopic image segmentation,[36] atomic and mesoscopic image segmentation from electron and scanning probe microscopy,[37] and three-dimension structures synthetization from two-dimension micrographs in material characterization.[38] However, there have been no studies on parsing microscopy imaging problems caused by inho-

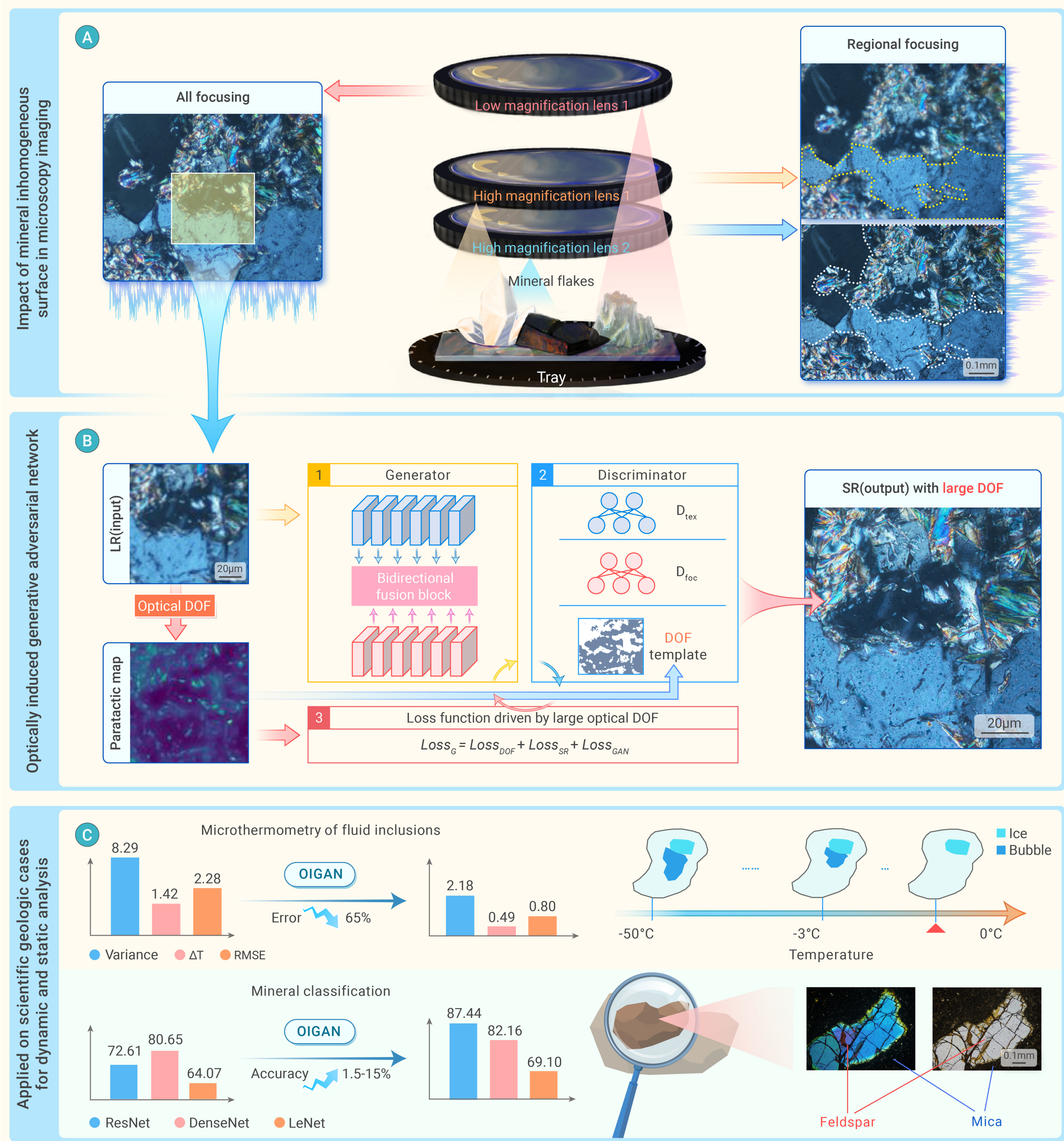

Figure 1. OIGAN utilizes optical DOF information to neutralize the impact of mineral inhomogeneous surface in mineral microscopy imaging (A) The imaging process of minerals in thin sections. Minerals with varying hardness in thin sections are difficult to grind into a consistently smooth microsurface, as shown in the middle. According to the principle of microscopy imaging, images from high magnification objective lens are prone to regional focusing with low DOF, as shown on the right. While images from low magnification objective lens have all focusing performance, as shown on the left. (B) Overall structure of proposed OIGAN. With optical DOF paratactic maps, OIGAN balances the contradiction between DOF and resolution aggravated by rough surface in mineral microscopy imaging. (C) Apply OIGAN in microthermometry of fluid inclusions and mineral classification to improve accuracy.

mogeneous surface phenomena in minerals using deep learning approaches. On the one hand, mineral microscopic images have great randomness due to irregular constituent spatial distribution and varying hardness of minerals. On the other hand, mineral microscopy imaging under polarized light is complex and nonlinearly affected by the optical properties of minerals, such as birefringence. In neural networks, massive parameters, dense layers and nonlinear activation functions are helpful in addressing above mentioned problems. Therefore, a deep learning method could be well-suited to optimizing the quality of mineral microscopic images.

In this study, it is observed that optical DOF information from low-magnification lens is the oracle for extended DOF resolution enhancement imaging and can provide robust prior knowledge for guiding neural networks to achieve extended DOF. Consequently, we proposed an optical-induced strategy of learning DOF from low-resolution images to guide deep-learning-based method, termed optically induced generative adversarial network (OIGAN) in Figure 1B (details in Methods). The proposed OIGAN model gives a physic-induced way to design deep learning networks. Meanwhile, we constructed a mineral microscopy dataset comprising 233,156 images from 115,346 pairs of low- and high-resolution images, involving three rock species (metamorphic rocks, sedimentary rocks and magmatic rocks). OIGAN can simultaneously achieve extended DOF and resolution enhancement. Further, the proposed OIGAN performed robustly on a wide range of minerals and optical conditions, surpassing the capability of existing methods. We also applied OIGAN to two scientific geologic cases for dynamic and static analysis: microthermometry of fluid inclusion and mineral classification (Figure 1C). The experiments show that OIGAN can facilitate the self-identification of minerals, automatic microthermometry of fluid inclusions and other tasks via microscopy.

MATERIALS AND METHODS

Optically induced generative adversarial network (OIGAN)

To generate images in accordance with human perception, generative adversarial network (GAN)-based methods have played a role in single image super-resolution task recent years. Super-resolution GAN (SRGAN) first proposed GAN-based network to achieve $4\times$ photo-realistic super-resolution and a perceptual loss calculated on feature maps of VGG (Visual Geometry Group) network.[39] To recover high-frequency edge details in remote sensing imaging, edge-enhancement GAN (EEGAN) proposed a two-serial-module GAN-based network: Ultradense subnetwork (UDSN) generated intermediate SR results with high resolution. Then Edge-enhancement subnetwork (EESN) enhanced edges of intermediate results by using Laplacian operator.[40] To improve perceptual effects, SRGAN with Ranker (RankSRGAN) proposed a trainable siamese network – Ranker.[41] It overcame the problem that most no-reference image quality assessment (NR-IQA) metrics are non-differentiable to be loss functions. Other CNN-based methods have also made efforts for image super-resolution.[42-45] Hierarchical dense recursive network was proposed to acquire multi-scale features and reconstruct features by global fusion module.[42] Multiscale deformable convolution alignment module was proposed to alleviate the information alignment difficulties.[43] CycMuNet+ proposed a mutual learning strategy to improve performance by spatial-temporal correlations.[44] Contrastive learning is utilized to learn the complicated degradations representations in embedding space and solve blind image super-resolution task.[45] In this study, we propose a dual-branch GAN-based method to introduce DOF information and achieve human perceptual-adaptive extended DOF resolution enhancement imaging performance.

The conflict between microscopy resolution and DOF is significantly reflected in the inhomogeneous surface of thin sections, which affects the overall quality of mineral microscopic images. We found that the wonderful large DOF information of low-resolution images is the key to achieve resolution enhancement reconstruction with extended DOF, further optimizing the quality of imaging results and breaking the shackles between resolution and depth of field in microscopic imaging. To neutralize the impact of mineral inhomogeneous surface in mineral microscopy imaging, we proposed optically induced generative adversarial network (OIGAN). The network consists of a generator G and two discriminators D_{foc}, D_{tex}, as shown in Figure 2A. The generator G contains dual branches to realize resolution enhancement reconstruction and extended DOF synchronously. Optical DOF information is introduced in generator G, discriminator D_{foc} and loss function, without requirement of extended DOF high-resolution data for supervision. Comparing with original SRGAN, our method adds a new branch in generator and a discriminator for extended DOF. Comparing with EEGAN, our method uses a parallel two-branch generator but not serial to achieve extended DOF and resolution enhancement simultaneously. Comparing with RankSRGAN, our method employs a dual-branch architecture without weight sharing and incorporates DOF information in loss function to achieve high DOF performance.

With I_{LR}, I_{HR} and I_{SR} representing low-magnification mineral microscopic image, high-magnification mineral microscopic image and reconstructed result, optimization objective G^* for the generator is represented by the following formula:

$$G^* = argmin\left(Div\left(I_{HR}, I_{SR}\right) + Div\left(\Delta d_S, \Delta d_L\right)\right), \tag{2}$$

where Δd_S and Δd_L represent the DOF of reconstructed image and low-resolution image, respectively. We constructed an algorithm denoted by C to extract optical DOF paratactic map F_{LR} and record the characteristic of low DOF. The optimization goal changes as follows:

$$G^* = argmin\left(Div\left(I_{HR}, I_{SR}\right) + Div\left(C\left(I_{SR}\right), C\left(I_{LR}\right)\right)\right). \tag{3}$$

To achieve this optimization goal, OIGAN implements optical DOF paratactic map as tutor in the three basic building blocks of GAN (generator, discriminator and loss function). Changes of the network were as shown in the following equations:

$$\begin{gathered} G\left(I_{LR}\right) \rightarrow G\left(I_{LR}, C\left(I_{LR}\right)\right), \\ D\left(I_{HR}, I_{SR}\right) \rightarrow D\left(I_{HR}, C\left(I_{HR}\right), I_{SR}, C\left(I_{SR}\right)\right), \\ loss_{SR} + loss_{GAN} \rightarrow loss_{DOF} + loss_{SR} + loss_{GAN}. \end{gathered} \tag{4}$$

Optical DOF information is integrated into the generator, discriminators and loss function of the OIGAN, which can achieve weak supervised learning only by high-magnification images with low DOF. Such optical DOF preservation and resolution enhancement similarity mutual learning structure allow OIGAN to turn fighting into ploughshares, with the ability to reconstruct mineral microscopic images with both large DOF and high resolution.

Constructing optical DOF paratactic map. The regions within the DOF of a mineral microscopic image have more details than the regions beyond. Through blurring filtering and difference calculation, these details can be extracted to record the DOF characteristics of different images. Therefore, we constructed the optical DOF paratactic map of microscopic image I through guided filtering algorithm based on blurring difference as directed graph RFM. With (x, y) represent position of the pixels, RFM is computed as:

$$\begin{gathered} M(x, y) = I(x, y) \times f_m, \\ RFM(x, y) = \left|I(x, y) - M(x, y)\right|, \end{gathered} \tag{5}$$

where f_m represents the mean blur kernel and $\times$ stands for convolution operation. Guided filtering not only has the advantages of effective edge preservation and non-iterative computation of bilateral filtering, but also reduces the computational complexity to O (1) order of magnitude.[46] Set i to represent the position of a pixel, ω_k to represent the local window, I, F, N, RFM to represent the input image, output image, noise, and guided map. The algorithm considers that a point on the function is a linear combination of adjacent points, thereby expressing a complex function through the average value of a series of local linear functions:

$$\begin{gathered} F_i = a_k RFM_i + b_k, \forall i \in \omega_k, \\ F_i = I_i - N_i, \end{gathered} \tag{6}$$

where a_k, b_k are constant coefficients, and ε is a regularization parameter. The guided filter optimization goal is to calculate appropriate parameters, reduce noise, and make the input image I closest to the output image F. After derivation, the constant coefficient calculation formulas are as follows:

$$\begin{gathered} a_k = \frac{\frac{1}{\omega}\sum_{i \in \omega_k}\left(RFM_i I_i - \mu_k \overline{I_k}\right)}{\sigma_k^2 + \varepsilon}, \\ b_k = \overline{I_k} - a_k \overline{\mu_k}, \end{gathered} \tag{7}$$

where μ_k and σ_k^2 represent the mean and variance of RFM in window ω_k. $\overline{I_k}$ represents the mean of the input image I in window ω_k. ω represents the total number of pixels. In order to avoid the multiple convolution computations in guided filtering algorithm from affecting the reconstruction of image edge, we reduced the kernel size to 3 and selected training images with a size of no less than 256 pixels.[46]

Optically induced dual-branch generators connected via bidirectional biased fusion module (BBFM). The generator has a parallel dual-branch

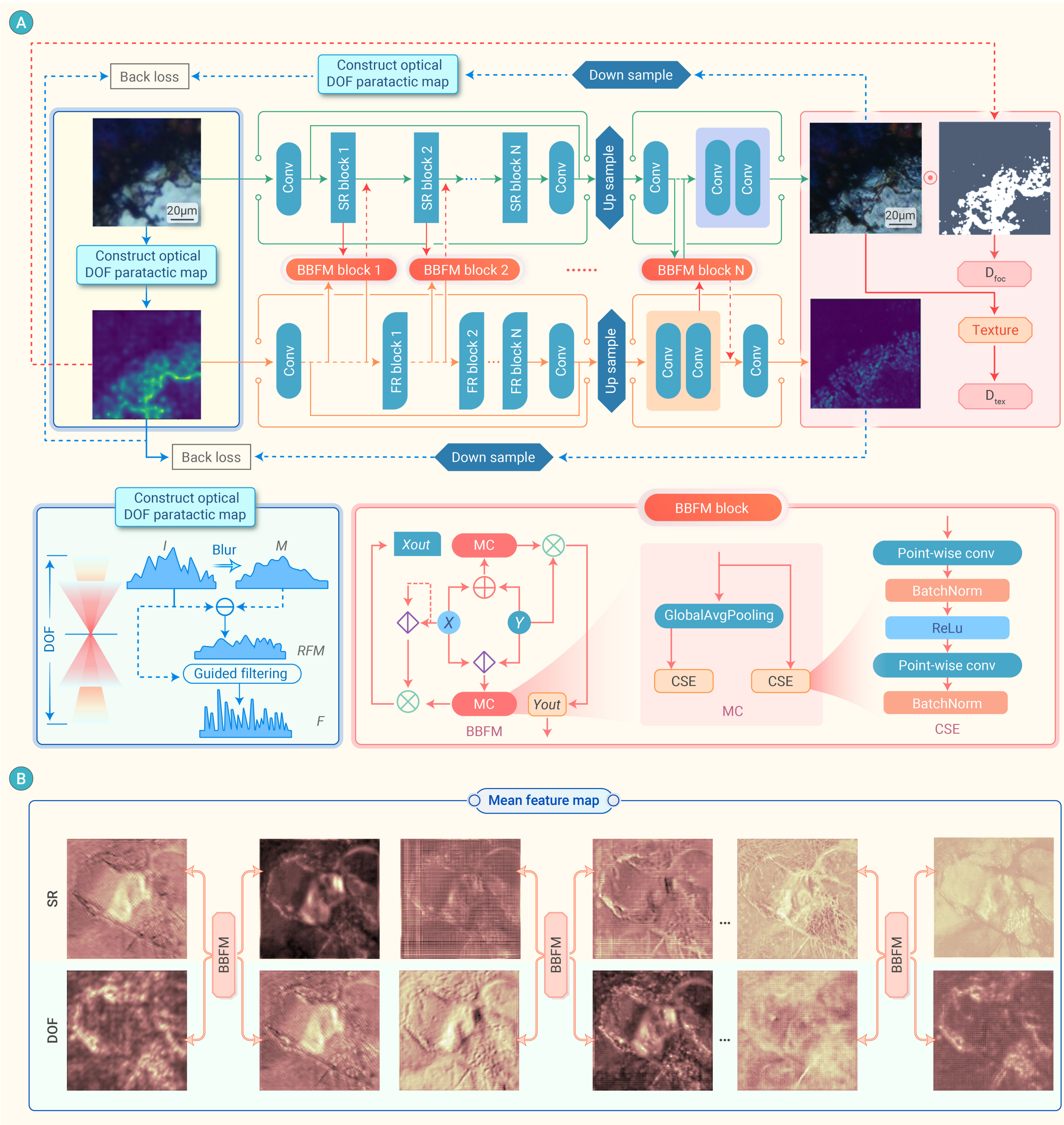

Figure 2. Optically induced generative adversarial network (A) Details of our proposed OIGAN. the low-resolution image and its optical DOF information permeate each other in the process of forward derivation, and further constrain each other in the backward propagation. (B) The features belong to each layer of the network before and after fusion by BBFM.

structure, including resolution raising branch and DOF estimation branch.

$$I_{SR} = G\left(I_{LR}, C\left(I_{LR}\right)\right), \tag{8}$$

As the formula shows, the generator has two inputs. In resolution raising branch, the low-resolution image input is reconstructed into high-resolution image. Synchronously, the DOF estimation branch reconstruct the DOF under high magnification lens based on the optical DOF paratactic map belonging to low-resolution image. In order to effectively induce resolution enhancement reconstruction through low magnification optical DOF feature, it is necessary to fuse the intermediate features of two branches in the forward propagation of network. Traditional information fusion methods are mostly simple addition or splicing according to dimension, which not only loses information but also provides insufficient guidance. We designed a self-attention bidirectional biased feature fusion module BBFM to carry out the information exchange between two branches and fully excavate the intermediate features of the two branches at different layers (Supplementary Algorithm 1). BBFM module includes two MC (Multi-scale Channel) calculations,[47] which generate self-supervised attention based on both local and global information. Supplemented by trainable weights, BBFM realizes bidirectional biased regulation of the network. BBFM makes the two branches complement and promote each other by realizing sufficient information exchange between them. Such fully communicated parallel structure effectively suppresses the region blurring caused by inhomogeneous surface and low DOF while increasing resolution.

Modulating the discriminator input with optical DOF paratactic map as template. SR image reconstructed through generative adversarial network has excellent visual perception, but may contain artifacts deviating from the real image[48] due to the complex texture of thin sections, which are composed of cracks and various mineral components. Two discriminators of the network, D_{foc} and D_{tex}, are used to suppress artifacts and produce more realistic textures. D_{foc} is used to determine the authenticity of the generated image. To suppress artifacts while extending the DOF of SR image, optical DOF template is added in front of the discriminator D_{foc} as:

$$D_{foc}(I_{HR}, I_{SR}) \rightarrow D_{foc}(I_{HR} \cdot T(C(I_{LR})), I_{SR} \cdot T(C(I_{SR}))), \tag{9}$$

where T is the threshold function. Template with true large DOF information effectively ensure the reliability of the texture from generated extended DOF images. D_{tex} computes the gradient information through function A:

$$D_{tex}(A(I_{HR}), A(I_{SR})), \tag{10}$$

which further improve the texture accuracy of the generated image.

Loss function driven by large optical DOF characteristics. The loss function of generator consists of three parts: optical DOF balanced loss function, SR constrained loss function and generative adversarial loss function. Therefore, loss function of the generative network $loss_G$ is defined as follows:

$$loss_G = loss_{DOF} + loss_{SR} + loss_{GAN}. \tag{11}$$

Among them, the optical DOF balanced loss function is used to make DOF of the reconstructed result closer to the input low-resolution image:

$$\begin{aligned} loss_{DOF} &= \beta_1 loss_{foc_s} + \beta_2 loss_{foc_b}, \\ loss_{foc_s} &= E_{I_L} \| C(I_{LR}) - C(DS(G(I_{LR}))) \|, \\ loss_{foc_b} &= E_{I_L} \| C(I_{LR}) - DS(G(C(I_{LR}))) \|, \end{aligned} \tag{12}$$

where $loss_{foc_s}, loss_{foc_b}$ respectively represent resolution raising branch balance loss function and DOF estimation branch balance loss function. β_1 and β_2 are 0.01 and 0.5. $G(I_{LR}), G(C(I_{LR}))$ are the outputs of two branches in OIGAN. DS is the down-sampling algorithm.

SR constrained loss function includes the pixel-level MSE loss function $loss_{pixel}$ and perceptual loss function $loss_{lpips}$, which are used to optimize the pixel-level realism and perceptual effect of the network respectively. $loss_{lpips}$ measures the similarity by calculating MSE of the features extracted by trained VGG network φ:

$$\begin{aligned} loss_{SR} &= \alpha_1 loss_{pixel} + \alpha_2 loss_{lpips}, \\ loss_{pixel} &= E_{I^L} \| G(I_{LR}) - I_{HR} \|, \\ loss_{lpips} &= E_{I^L} \| G(\varphi(I_{LR})) - \varphi(I_{HR}) \|, \end{aligned} \tag{13}$$

where α_1, α_2 are constant parameters with values 0.5 and 1.

Generative adversarial loss function includes the training interaction with the two discriminators:

$$loss_{GAN} = \gamma_1 loss^G_{adv_f} + \gamma_2 loss^G_{adv_t}, \tag{14}$$

where $loss^G_{adv_f}$ and $loss^G_{adv_t}$ are adversarial loss function with D_{foc} and D_{tex}, respectively. γ_1 and γ_2 are 0.05 and 0.005.

Loss function of the discriminator network includes $loss^D_{foc}$ of the resolution enhancement reconstruction discriminator D_{foc} and $loss^D_{tex}$ of the texture reconstruction discriminator D_{tex}.

RESULTS

Mineral microscopic image dataset

We built a dataset consisting of different rocks, microscopy modes and different DOF for evaluating performance of extended DOF resolution enhancement imaging and generalization. The dataset contains 233,156 mineral microscopic images, which includes 115,346 aligned pairs of low- and high-resolution images. Low-resolution images with size of 128×128 pixels were acquired using a 5×/0.15-NA objective lens. High-resolution images with size of 512×512 pixels were acquired using a 20×/0.45-NA objective lens. Details about acquisition and quantitative information of the dataset are provided in Supplemental Information.

The whole dataset is divided into four parts according to different characteristics (Table S1, Figures S1 & S2). Dataset D is an all-focus dataset built for evaluating performance of extended DOF resolution enhancement imaging, constituted by cross-polarized images of marble. Each group of data in Dataset D contains three images: low-resolution (LR) microscopic image, high-resolution (HR) microscopic image with regional focus, and fused (FU) full-focus microscopic image. LR and HR images are used for training, FU images are only used for testing. Datasets B and C are built for evaluating generalization of microscopy modes, with paired LR and HR images. Dataset C is a plane-polarized light microscopic image dataset of olivine, constituted by images relatively single in color. Dataset B is a cross-polarized light microscopic image dataset of olivine, containing images with diverse and complex colors according to interference phenomenon produced by the birefringence property of minerals. Dataset A is built for evaluating generalization of different rocks, containing cross-polarized microscopic images from all three types of rocks (metamorphic rocks, sedimentary rocks and magmatic rocks).

Evaluation metrics and comparison methods

To effectively evaluate the performance of various methods, a series of credible image quality assessment measures were applied. Among them, peak signal-to-noise ratio (PSNR) and root mean squared error (RMSE)[49] are calculated based on mean squared error (MSE) between images and are sensitive to pixel-wise errors. Images with larger PSNR or smaller RMSE values are more similar to the reference images and with better quality. Learned Perceptual Image Patch Similarity (LPIPS)[50] fills the gap of perception similarity evaluation indicators which provides discrimination results close to human perception standards through big data-driven networks. Fréchet Inception Distance (FID)[51] measures the similarity of two groups of images based on the statistical results of visual features. Perception index (PI) combines two no-reference image quality measures.[52] Images with low LPIPS, FID and PI have good perceptual effects and quality. Deep-learning based methods (ESRGAN,[53] USISGAN,[54] DUSGAN[55] and Beby-GAN[48]) were used for comparison.

Achieving high-quality extended DOF resolution enhancement imaging on mineral microscopy data

Experiments on our constructed mineral datasets were conducted to evaluate the performance of SR methods by visual results, quantitative results, subjective survey, physical verification, geological benefits and interpretability analysis. HR data from Datasets A-C and FU data from Dataset D were used to test the extended DOF resolution enhancement imaging and generalization performance of methods for different microscopy modes and minerals.

Visual results. Figure 3A shows visual results of different methods on both cross-polarized light (left) and plane-polarized light (right). USISGAN and DUSGAN generate blurry visual results similar to LR images, which demonstrates that only utilizing high-frequency details to achieve unsupervised SR does not work well in mineral microscopy imaging. ESRGAN generates clear SR results but with bubble-like artifacts or color distortion. Beby-GAN shows good SR results similar to HR images by utilizing the best-buddy loss to relax the immutable one-to-one constraint. However, tessellated textures exist in SR results of Beby-GAN, and are more obvious under plane-polarized light. OIGAN keeps the authenticity of color well and has the clearest mineral textures on both cross-polarized light and plane-polarized light comparing with other methods. Meanwhile, more visual results of different minerals are shown in Figure S3. Mineral particle boundaries in thin sections, such as quartz and olivine, are clear to separate minerals easily. Cleavage of mica, cracks of olivine, polysynthetic twin of plagioclase are clear to be identified. Further, the optical DOF feature maps of LR data, HR data and reconstructed results are shown below the corresponding microscopic images. From the

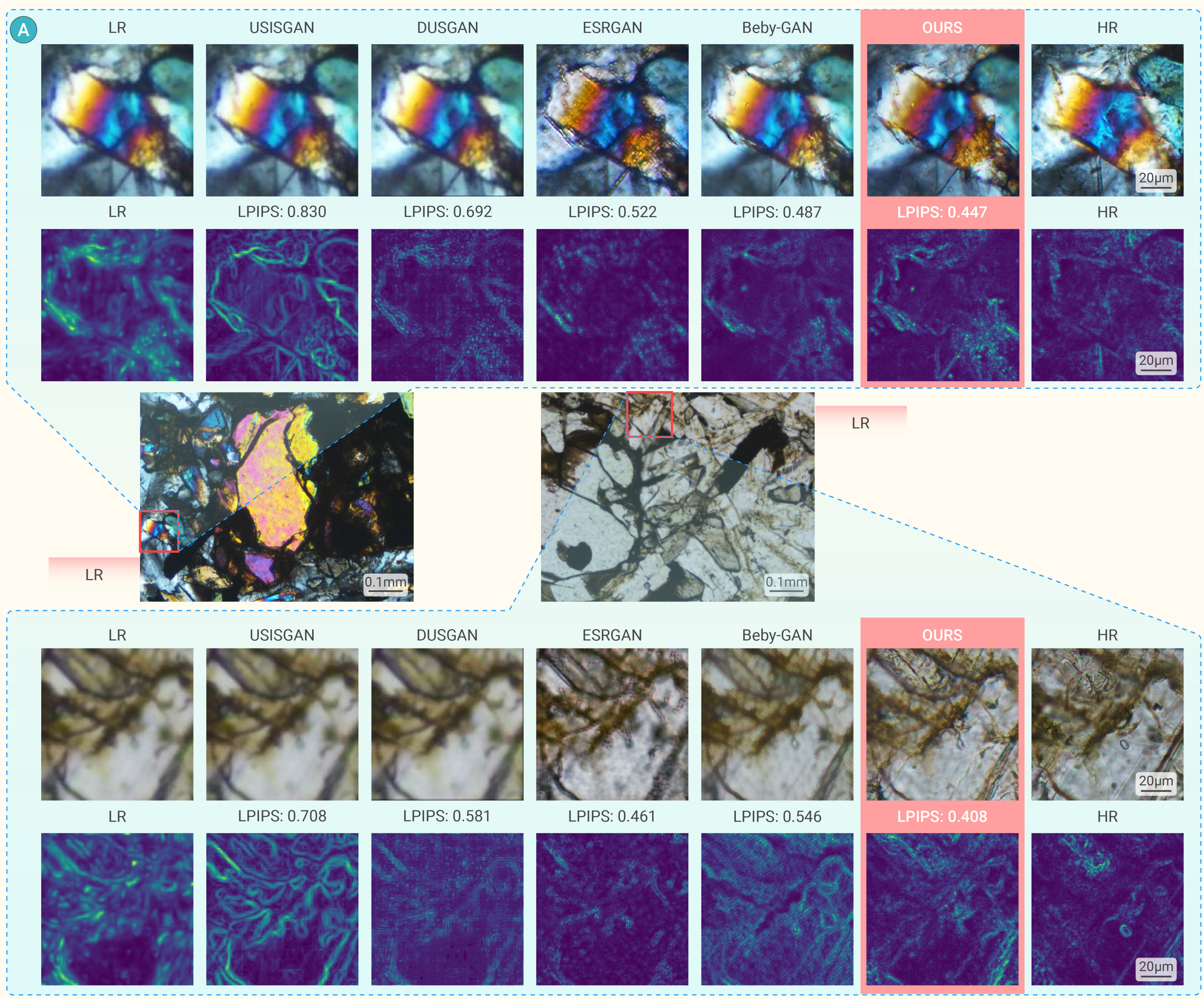

B

Subjective score			
	Cross polarized	Plane polarized	Overall test data
USISGAN	0.0014	0.0008	0.0012
ESRGAN	0.5992	0.1968	0.3778
DUSGAN	0.0104	0.0039	0.0079
Beby-GAN	0.0988	0.0929	0.1037
OIGAN	1	1	1

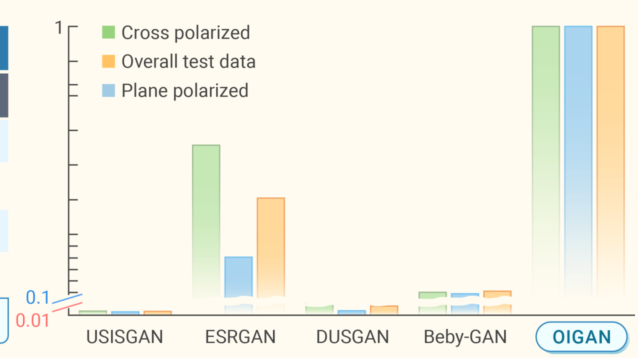

Figure 3. OIGAN achieves high-quality extended DOF resolution enhancement imaging on mineral microscopy data (A) Visual results and optical DOF feature maps of different methods. (B) Subjective scores of different methods.

optical DOF feature maps, LR data has high attention values in the whole area, which shows good focus performance with large DOF. HR data has high attention values only in partial areas, which is limited by DOF. Results constructed by USISGAN and DUSGAN also have banded artifacts while results constructed by ESRGAN show a limited DOF. SR results of Beby-GAN under plane-polarize light have evenly distributed optical DOF feature maps but these calculated focused areas are from tessellated textures in the image, not mineral textures. The optical DOF feature maps of OIGAN are evenly distributed in the whole image comparing with HR images, which demonstrates the capability of extending DOF.

Visual results of Dataset D demonstrated in Figure S4 further evaluate the ability of OIGAN to construct resolution enhancement mineral microscopic images with large DOF. Experiments on Dataset D used HR images as weak-supervised labels in training, while FU images with large DOF were used as

Table 1. Image quality assessment on benchmarks

Dataset	Metric	USISGAN	ESRGAN	DUGAN	Beby-GAN	OURS
	PSNR↑	18.93	18.28	18.85	19.10	**19.25**
	RMSE↓	28.49	28.29	28.84	27.51	**25.49**
Dataset A	LPIPS↓	0.663	0.444	0.604	0.416	**0.413**
	FID↓	82.83	**15.99**	106.77	20.12	19.01
	PI↓	8.21	6.72	9.78	7.33	**6.68**
	PSNR↑	18.65	18.30	18.60	19.15	**19.19**
	RMSE↓	27.54	26.97	27.88	25.88	**24.59**
Dataset B	LPIPS↓	0.653	0.441	0.606	0.416	**0.378**
	FID↓	84.46	22.75	101.61	24.41	**10.25**
	PI↓	8.15	**6.66**	9.80	7.27	6.81
	PSNR↑	18.75	17.74	18.72	19.44	**19.46**
	RMSE↓	27.68	29.71	27.85	25.05	**24.16**
Dataset C	LPIPS↓	0.759	0.474	0.672	0.498	0.403
	FID↓	133.22	46.57	153.95	47.41	**24.18**
	PI↓	8.42	**6.82**	10.11	7.31	7.21
	PSNR↑	17.41	17.98	17.38	20.53	**22.07**
	RMSE↓	35.40	32.51	35.67	23.06	**17.69**
Dataset D	LPIPS↓	0.702	0.464	0.670	0.508	**0.434**
	FID↓	119.65	49.34	174.13	64.99	**28.24**
	PI↓	8.478	**7.00**	10.00	7.26	7.25

'↓' means the lower, the better. '↑' indicates the higher, the better.

references in testing. Results of USISGAN and DUSGAN on Dataset D excessively inherit the characteristics of LR images, which negatively impacts the clarity of their optical DOF feature maps. The bubble-like artifacts of ESRGAN results aggravate the deformation of the optical DOF feature maps. Beby-GAN is deficient in the restoration of mineral fractures while possesses optical DOF feature maps close to HR. The reconstruction results and optical DOF feature maps of OIGAN are more similar to FU images, compared with other methods. The generated images close to FU demonstrate that our method successfully learns the DOF information missed in the training HR data. The design in OIGAN of utilizing DOF information from LR data helps to extend DOF effectively.

In our comparison experiments, we further applied image sharpening algorithms through edge enhancement (High-Boost Filtering,[56] Laplacian Filtering,[57] and Laplacian of Gaussian (LoG)[58]) to discern the differences between boundary enhancement and our method (Figure S5). While all three methods effectively enhance edges, the images generated using the High-Boost and Laplacian filter methods exhibit noticeable noise. The LoG method mitigates this issue by employing Gaussian filtering before applying the Laplacian filter, resulting in a sharpened image with superior visual effects. However, it is crucial to note that these methods primarily emphasize existing edges in low-resolution images. They fall short in producing fine and clear mineral textures and are unable to distinguish overlapping diffraction patterns in low-resolution images.

Quantitative results. Quantitative results are shown in Table 1. The values of metrics are mean values of the data in each dataset. On Dataset A, USISGAN and DUSGAN have poor perceptual performance with LPIPS and FID at least 36% higher than other methods. ESRGAN has good perceptual performance with the best FID 15.99, the second best LPIPS and PI, but performs poorly on PSNR and RMSE. Beby-GAN and OIGAN show excellent performance on both pixel and perceptual metrics. Our OIGAN has the best PSNR 19.25dB, which demonstrates generalization performance on different minerals. On Dataset B, all metrics keep similar values to Dataset A, because both datasets are acquired using cross-polarized light. OIGAN shows good performance on most metrics, at least 54% decrease on FID than other methods. On Dataset C, USISGAN and DUSGAN show significant reducing performance on perceptual metrics comparing with Dataset B (at least 10% increase on LPIPS and 47% increase on FID). PSNR of ESRGAN decreases about 0.5dB comparing with Dataset B. Beby-GAN and OIGAN perform stably under both plane-polarized light and cross-polarized light. Metrics have low fluctuations between Datasets B and C, which shows the adaptability of Beby-GAN and OIGAN for different polarization states. Experiments on Dataset D used FU images with large DOF as references. OIGAN achieves at least a 42% decrease on FID and 1.54dB increase on PSNR. PSNR (22.11dB) and RMSE (17.69) of OIGAN are the best compared with other methods, which shows good pixel-level similarity. Further, pixel-level metrics of OIGAN perform better on Dataset D than on other Datasets. PSNR of OIGAN increased 2.81dB on Dataset D comparing with the mean value of Datasets A-C (19.3dB), while PSNR of other methods decreased except Beby-GAN. PSNR of Beby-GAN increased 1.3dB on Dataset D, about 47% of OIGAN. RMSE of OIGAN decreased 24% on Dataset D comparing with the mean value of Datasets A-C (24.75), while RMSE of other methods increased except Beby-GAN. This phenomenon shows the capability of OIGAN for extending DOF, which demonstrates that OIGAN can neutralize the conflict between large DOF and high-resolution in mineral microscopy imaging by introducing DOF information. In general, from experiments on four parts of dataset, OIGAN maintains the best quantitative performance on pixel measures while achieving excellent perceptual measures, which demonstrates good generalization on different minerals with both cross-polarized and plane-polarized light.

Subjective survey. Given the limitations of current objective evaluation systems for mineral microscopy imaging, mainly in relation to sharpness, a subjective survey is necessary to validate the effectiveness of enhancement for mineral textures. The SR results obtained from different methods were randomized and sampled in pairs for comparison. Human participants were asked to choose which image is of high quality from each pair by a released

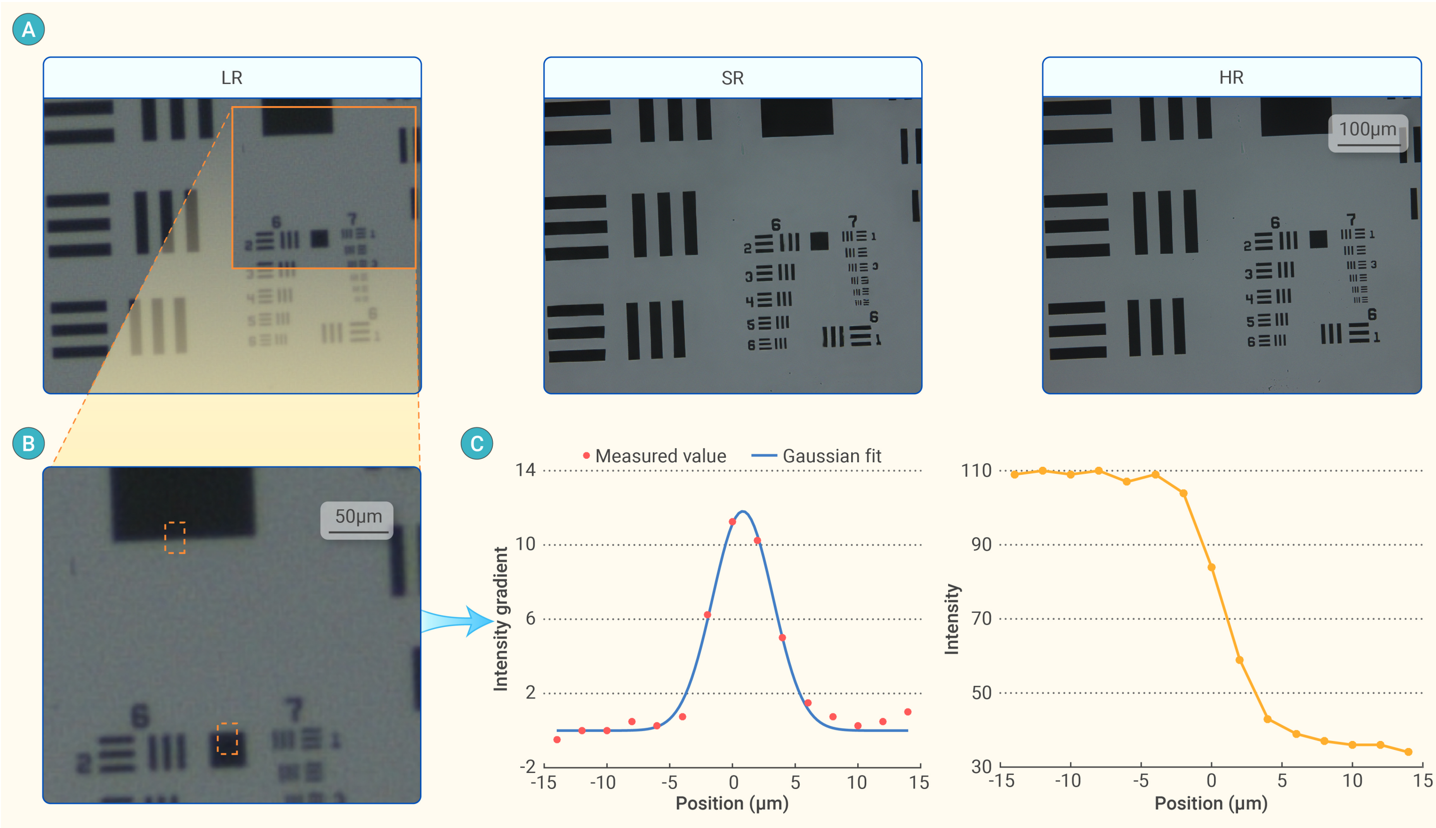

Figure 4. Physical verification and geological benefits of extended DOF resolution enhancement imaging achieving by OIGAN (A) OIGAN achieves high-quality resolution enhancement results on calibration plate. (B) USAF 1951 Square edge image selection, represented by blue boxes. (C) Intensity distribution crossing the edge and corresponding intensity gradient. The green line is the curve of pixel value distribution. The red dots are gradient values and the blue line is the curve fitted by the Gaussian model.

software.[59] The survey included 4,800 pairs of images and there were 24 human participants from Peking University and Beihang University. Each human participant compared 200 pairs. The comparison results were fitted using the Bradley-Terry model[60] to obtain a true rating for each method. We verified the performance of all methods on plane-polarized light and cross-polarized light data. Subjective scores (denoted as S) are shown in Figure 3B. The subjective scores of OIGAN are substantially higher than the other methods, which is at least 66% better than other methods (the second best: ESRGAN on cross-polarized light data, 0.5992). Other methods suffer performance degradation on plane-polarized light data with a decrease of subjective scores, while OIGAN performs stably on both plane-polarized light and cross-polarized light data.

Physical verification. To physically verify the effective performance of the proposed OIGAN for resolution enhancement, we adopt the widely used USAF 1951 Test Target (THORLABS A10S1P) with line pairs to estimate the Point Spread Function (PSF) of the LR, SR and HR imaging systems (Figure 4A).[61] The resolution is specified in line pairs per millimeter (lp/mm) by group number (G) and element umber (E). The largest set of non-distinguishable horizontal and vertical lines determines the resolving power (R) of the imaging system. Based on USAF 1951 test target, knife-edge method is adopted for PSF estimation.[62] Under the assumption that the distribution of PSF follows isotropic two-dimensional Gaussian distribution, the PSF size along one axis could be quickly estimated by fitting the standard deviation σ in the Gaussian distribution. The spot size is its full width at half maximum (*FWHW*), which is the width from 12% to 88% of the cumulative distribution function and can be calculated as follows:

$$FWHW = 2\sqrt{2\ln 2}\sigma \approx 2.355\sigma. \tag{15}$$

As shown Figure 4A, the largest distinguishable set in LR image is G6E6 with 114 lp/mm. In SR and HR images, the largest distinguishable set is G7E6 with 228 lp/mm. The edges of the square on the USAF 1951 test target are used to calculate the PSF size (orange boxes in Figure 4B). The corresponding intensity distribution and intensity gradient are shown in Figure 4C. The intensity gradient of the square edge denotes the shape of the light spot. Therefore, the PSF could be estimated by fitting the standard deviation σ in the Gaussian distribution. In order to reduce errors, the estimated PSF from four edges are averaged. For LR image, the mean spot size is 7.998 μm. For SR image, the mean spot size is 1.344 μm. For HR image, the mean spot size is 1.358μm. Results of test target physically verify the resolution enhancement capability of OIGAN. SR result of OIGAN keeps good image clarity and has similar PSF size with HR.

Geological benefits. OIGAN can effectively improve the observing and judging effects towards the morphological and optical features of minerals, including the ultra-fine morphology, cleavage, relief, extinction and interference, under both plane-polarized and cross-polarized lights. In Figure 5, six groups of mineral features are indicated by arrows in LR images (left) and SR results of OIGAN (right). As shown in Figure 5A, it is challenging to distinguish the number of inclusions in the LR images (indicated by blue arrows). However, by applying OIGAN, the phase boundaries are obviously sharpened to make the edge of each inclusion clearer (indicated by blue arrows in the right part), which is particularly useful in identifying small or tiny inclusions in minerals such as quartz. Moreover, OIGAN can also improve the contrast and recognition of transition colors of heterogeneous minerals, and thus helping to identify the characteristics of growth zones at different stages. As shown in Figure 5B, the color transition from light yellow to dark yellow is more distinctive (purple arrows from left to right). Similarly, in the right group of the second row, the transition from orange to brownish red is more apparent (purple arrows from left to right). In Figure 5C, the boundaries of different mineral phases are also easier to be identified after using OIGAN, such as garnet (pink arrows). The effectiveness of OIGAN is demonstrated in minerals with different sizes. Overall, OIGAN enables to solve the recognition problems of fine profiles and color features in LR images. These details can help to identify the subtle textural variations and deformational structures of rocks or minerals, which are essential for understanding their tectonic and metamorphic history, as well as interpreting the genetic mineralogy.

Interpretability analysis. The architecture of OIGAN and the features of

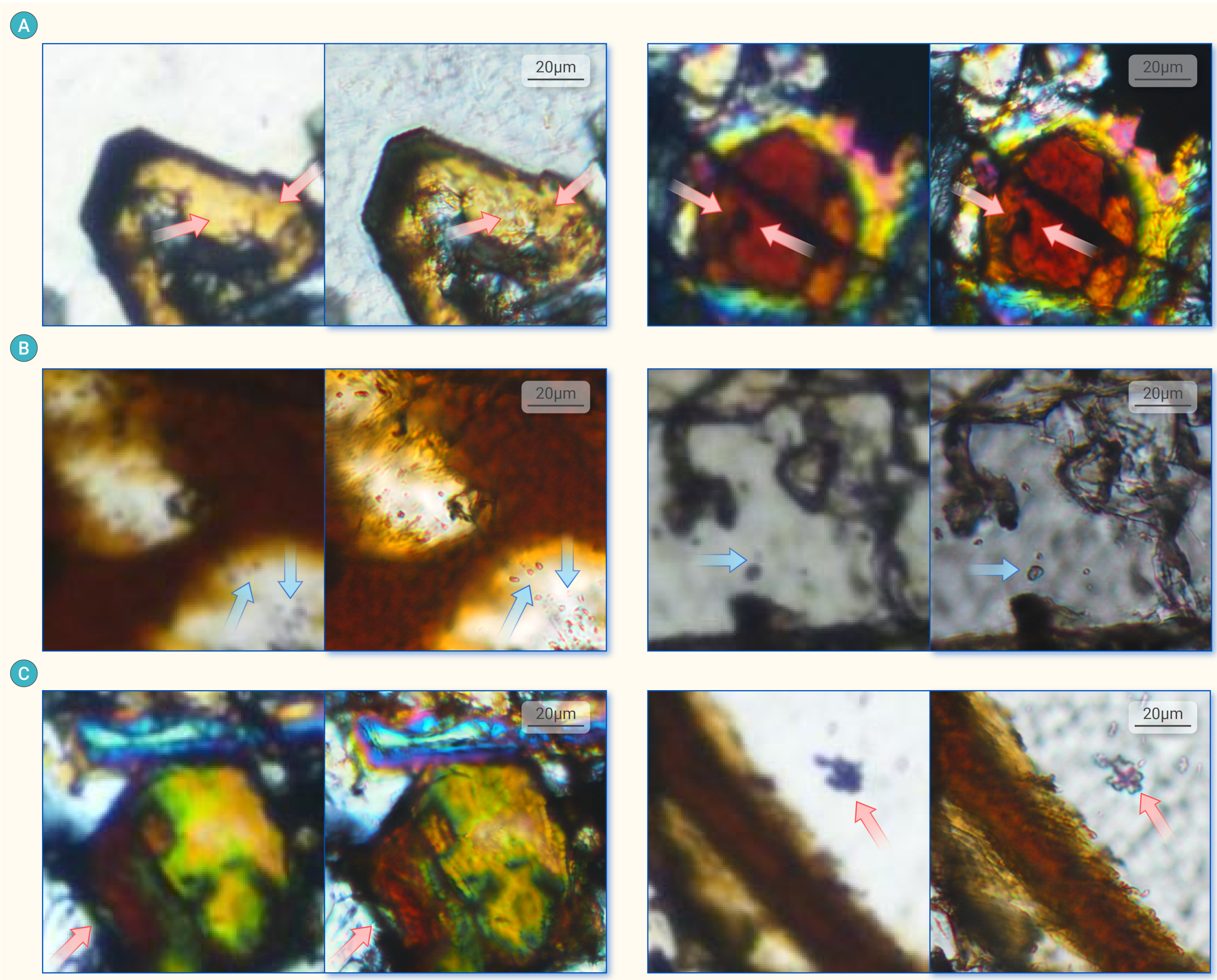

Figure 5. The mineral features of interest are indicated by arrows in LR images (left) and SR results of OIGAN (right) (A) Small inclusions are indicated by blue arrows. (B) Growth zones are indicated by purple arrows. (C) Mineral particle boundaries are indicated by pink arrows.

OIGAN belonging to each layer are shown in Figure 2A & B. Evolution of feature maps shows that the reconstruction of SR images by generator is a process of mutual learning between the upper and lower branches. DOF estimation branch with optical DOF paratactic maps as input provides the annotation of attention region for the resolution raising branch. Resolution raising branch with low-resolution images as input supplements the current image feature information for DOF estimation branch, so that the feature update of DOF estimation branch keeps up with the feature change of resolution raising branch. This mutual promotion mechanism enables the network to reconstruct images with high-resolution and large DOF characteristics simultaneously.

Making accurate ice-melting temperature measurement of fluid inclusions possible

To dig the potential application, OIGAN is applied on downstream tasks. Fluid inclusions in minerals consist of trapped gases, liquids or daughter crystal. Fluid inclusions provide indispensable information about geological processes, contributing to fundamental processes in geology, exploration for mineral deposits, gemology, analysis of air-inclusions in ice cores, petroleum exploration and so on.[63] In microthermometric study of fluid inclusion, geologists record ice-melting temperature by observing the phase transition of the fluid inclusion during the freezing and heating process with plane-polarized light. Fluid inclusions tremble with temperature changing constantly, so observations suffer from out-of-focus with 50× or 100× objective lenses. It is hard to get precise ice-melting temperature with 0.1 centigrade margin of error by persistent dynamic observation. Therefore, results of OIGAN are adopted to achieve accurate ice-melting temperature measurement of fluid inclusions (Figure 6). Pipeline of fluid inclusion experiments is shown in Figure 6A (Details in Supplementary Information). Quantitative and visual results are shown in Figures 6B & C.

Comparing fluid inclusions in FOV (Figure 6C), it can be seen that fluid inclusions in SR data had clearer outlines. According to magnification images in the top right corner of each fluid inclusion, the edges of bubbles and ice cubes were significantly refined, which are key marks for measuring the ice-melting temperature of fluid inclusions. Microthermometric results of LR and SR data were analyzed quantitatively on variance, ΔT and RMSE, as shown in boxplots of Figure 6B. Variance represents the variance value of results from different participants on the same fluid inclusion. ΔT represents the difference between ground-truth of a fluid inclusion with mean value of results from different participants on the same fluid inclusion. RMSE represents the root mean square error of results from different participants on the same fluid inclusion. Comparing variance of observations on LR and SR data, the mean variance of SR (2.183) is 74% lower than mean variance of LR (8.286), which means more stable performance is offered on SR data. The variance

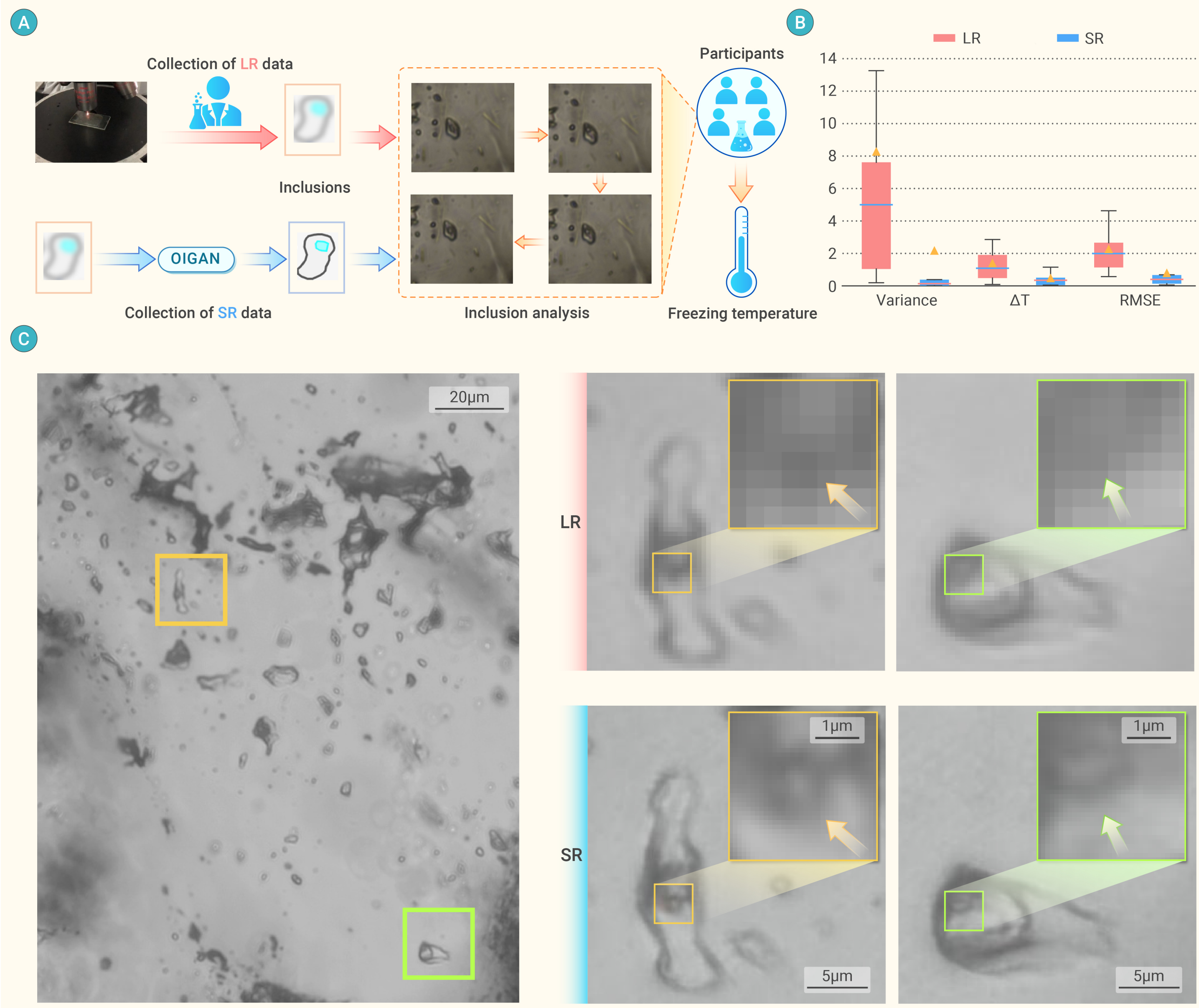

Figure 6. Microthermometry of fluid inclusions (A) Pipeline of fluid inclusion experiments. (B) Comparison of observing ice-melting temperature results from LR data and SR data on variance, ΔT, RMSE. (C) Comparison of images in LR and SR data on visual results. Magnification images of bubbles and ice cubes are located in top right corner of each fluid inclusion.

distribution on SR data is more centralized with a smaller box height, which demonstrates that the participants had similar judgments of ice-melting temperature on SR videos. Comparing with ground-truth, observations on SR data have lower mean values of ΔT and RMSE (0.489 and 0.802), which shows 65% decrease with observations on LR data (1.416 and 2.28). The accuracy of ice-melting temperature measurement has been significantly improved by OIGAN. The experiment shows that average observation values of ice-melting temperature on SR data are closer to ground-truth values and more stable. Results generated by OIGAN help participants achieve great precision.

Promoting for high performance of mineral classification

Mineral identification and ore identification are the basic means of geological research. Meanwhile, achieving mineral classification automatically by algorithms is directly influenced by the imaging quality of mineral microscopy. Results of OIGAN are adopted to promote mineral classification on constructed mineral classification dataset with 1993 images (Figures 7 & S8). Pipeline of mineral classification experiments is shown in Figure 7A (Details in Supplementary Information). Quantitative and visual results are shown in Figures 7B & C.

As shown in Figure 7C, textures of minerals were clearer after SR. For example, impurities on the surface of quartz and feldspar become easier to be observed on SR data, which can effectively help distinguish quartz from feldspar. Calcite with two cleavages and plagioclase with polysynthetic twin have similar features to be identified. OIGAN helps to magnify details of minerals for a clearer classification. Figure 7B shows the classification accuracy of LR and SR data. With resolution enhancement, average classification accuracy has risen 5% on LeNet, 15% on ResNet18 and 1.5% on DenseNet. Notably, classification probability on SR data was more centralized than on LR data. Fewer outliers appeared in the results of SR data compared with LR data. Our experiments indicate that the proposed computational imaging technology is helpful for mineral identification and other applications.

DISCUSSION

Due to the uneven microsurfaces of thin sections and conflict between DOF and resolution of microscopes, region blurring phenomenon caused by low DOF is significant in high magnification images. To fill in the gaps of neutralizing the impact of inhomogeneous surfaces in mineral microscopy

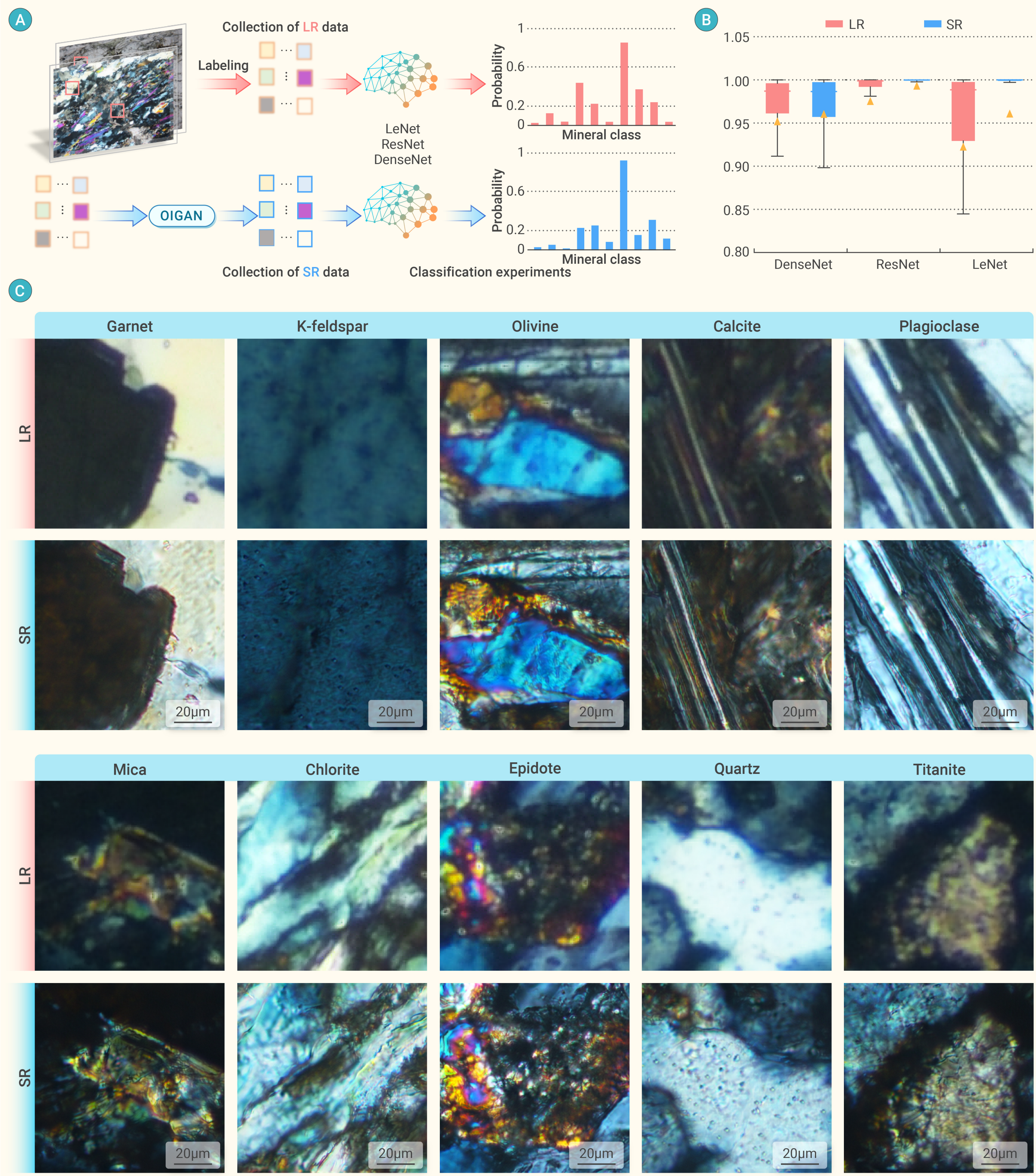

Figure 7. Mineral classification (A) Pipeline of mineral classification experiments. (B) Comparison of classification results. (C) Comparison of LR images and SR images on visual results.

imaging, we revealed that optical DOF information from low-magnification lens is the oracle for extended DOF resolution enhancement imaging. Building upon this discovery, we integrated this physical knowledge into deep learning, presenting an optically induced generative adversarial network (OIGAN) to infer extended DOF resolution enhancement data by acquiring optical DOF information from LR mineral microscopic images.

Meanwhile, a large-scale mineral microscopy dataset comprising 233,156 images with 115,346 pairs of low- and high-resolution images was constructed for model training and evaluation. Also, some deep learning image super-resolution approaches were applied to evaluate the generalizability and capability for capturing the patterns of complicated optical phenomena. OIGAN achieved the best performance on most metrics, which demonstrated our network is applicable to a wide range of minerals and optical conditions. More importantly, through experiments on Dataset D that are the closest to the real situation, OIGAN achieved the state-of-the-art performance, at least 42% decrease on FID and 1.54 dB increase on PSNR. Based on visual results, quantitative results, subjective survey, physical verification, geological benefits and interpretability analysis, the proposed OIGAN can achieve extended DOF and resolution enhancement simultaneously, which is beyond the capability of existing methods.

Specifically, different geologic cases (microthermometry of fluid inclusion and mineral classification) were tested, demonstrating the potential for assisting dynamic and static geoscience applications. The experiments shown that OIGAN can significantly improve the accuracy of fluid inclusion ice-melting temperature measurement with the mean error reducing 65% and assist mineral classification with 1.5%～15% increase in accuracy. It is believed that the proposed deep learning method is helpful to promote the self-identification of minerals under the microscope, accurate statistics of mineral content, discrimination of mineral morphology and growth environment, automatic microthermometry of fluid inclusions and so on. Moreover, OIGAN revealed an innovative way to design neural networks by integrating physical information from real-world. Also, it revealed the potential of computational imaging methods to overstep the limit of actual imaging system.

REFERENCES

1. Mitchell, R.N. (2021). Chang'E-5 reveals the Moon's secrets to a longer life. The Innovation **2**: 100177. DOI: 10.1016/j.xinn.2021.100177.
2. Chen, Y., Hu, S., Li, J.-H., et al. (2023). Chang'e-5 lunar samples shed new light on the Moon. The Innovation Geoscience **1**: 100014. DOI: 10.59717/j.xinn-geo.2023.100014.
3. Hell, S.W. and Wichmann, J. (1994). Breaking the diffraction resolution limit by stimulated-emission—stimulated-emission-depletion fluorescence microscopy. Opt. Lett. **19**: 780–782. DOI: 10.1364/ol.19.000780.
4. Gustafsson, M.G.L. (2000). Surpassing the lateral resolution limit by a factor of two using structured illumination microscopy. J. Microsc-Oxford **198**: 82–87. DOI: 10.1046/j.1365-2818.2000.00710.x.
5. Gustafsson, M.G.L. (2005). Nonlinear structured-illumination microscopy: Wide-field fluorescence imaging with theoretically unlimited resolution. Proc. Natl. Acad. Sci. USA **102**: 13081–13086. DOI: 10.1073/pnas.0406877102.
6. Rust, M.J., Bates, M., and Zhuang, X. (2006). Sub-diffraction-limit imaging by stochastic optical reconstruction microscopy (STORM). Nat. Methods **3**: 793–796. DOI: 10.1038/nmeth929.
7. Wang, Z., Zhao, T., Cai, Y., et al. (2023). Rapid, artifact-reduced, image reconstruction for super-resolution structured illumination microscopy. The Innovation **4**: 100425. DOI: 10.1016/j.xinn.2023.100425.
8. Schultz, R.R. and Stevenson, R.L. (1994). A Bayesian approach to image expansion for improved definition. IEEE T. Image Process **3**: 233–242. DOI: 10.1109/83.287017.
9. Schultz, R.R. and Stevenson, R.L. (1996). Extraction of high-resolution frames from video sequences. IEEE T. Image Process **5**: 996–1011. DOI: 10.1109/83.503915.
10. Chang, H., Yeung, D.-Y., and Xiong, Y. (2004). Super-resolution through neighbor embedding. In Proceedings of the 2004 IEEE Computer Society Conference on Computer Vision and Pattern Recognition. DOI: 10.1109/CVPR.2004.1315043.
11. Kim, K.I., Franz, M.O., and Scholkopf, B. (2005). Iterative kernel principal component analysis for image modeling. IEEE T. Pattern Anal. **27**: 1351–1366. DOI: 10.1109/TPAMI.2005.181.
12. Yang, J., Wright, J., Huang, T.S., et al. (2010). Image super-resolution via sparse representation. IEEE T. Image Process **19**: 2861–2873. DOI: 10.1109/TIP.2010.2050625.
13. Dowski, E.R. and Cathey, W.T. (1995). Extended depth of field through wave-front coding. Appl. Opt. **34**: 1859–1866. DOI: 10.1364/AO.34.001859.
14. Botcherby, E.J., Booth, M.J., Juškaitis, R., et al. (2008). Real-time extended depth of field microscopy. Opt. Express **16**: 21843–21848. DOI: 10.1364/OE.16.021843.
15. Jin, L., Tang, Y., Wu, Y., et al. (2020). Deep learning extended depth-of-field microscope for fast and slide-free histology. Proc. Natl. Acad. Sci. USA **117**: 33051–33060. DOI: 10.1073/pnas.201357111.
16. Wu, Y., Rivenson, Y., Wang, H., et al. (2019). Three-dimensional virtual refocusing of fluorescence microscopy images using deep learning. Nat. Methods **16**: 1323–1331. DOI: 10.1038/s41592-019-0622-5.
17. Luo, Y., Huang, L., Rivenson, Y., et al. (2021). Single-shot autofocusing of microscopy images using deep learning. ACS Photonics **8**: 625–638. DOI: 10.1021/acsphotonics.0c01774.
18. Dong, C., Loy, C.C., He, K., et al. (2015). Image super-resolution using deep convolutional networks. IEEE T. Pattern Anal. **38**: 295–307. DOI: 10.1109/DSC.2016.104.
19. Zhang, Y., Li, K., Li, K., et al. (2018). Image super-resolution using very deep residual channel attention networks. In Proceedings of the European Conference on Computer Vision (ECCV). DOI: 10.1007/978-3-030-01234-2_18.
20. Liang, J., Cao, J., Sun, G., et al. (2021). Swinir: Image restoration using swin transformer. In Proceedings of the IEEE/CVF International Conference on Computer Vision. DOI: 10.1109/ICCVW54120.2021.00210.
21. Ma, C., Rao, Y., Cheng, Y., et al. (2020). Structure-preserving super resolution with gradient guidance. In Proceedings of the IEEE/CVF Conference on Computer Vision and Pattern Recognition. DOI: 10.1109/CVPR42600.2020.00779.
22. Qiao, C., Li, D., Guo, Y., et al. (2021). Evaluation and development of deep neural networks for image super-resolution in optical microscopy. Nat. Methods **18**: 194–202. DOI: 10.1038/s41592-020-01048-5.
23. Wang, H., Rivenson, Y., Jin, Y., et al. (2019). Deep learning enables cross-modality super-resolution in fluorescence microscopy. Nat. Methods **16**: 103–110. DOI: 10.1038/s41592-018-0239-0.
24. Qiao, C., Li, D., Liu, Y., et al. (2023). Rationalized deep learning super-resolution microscopy for sustained live imaging of rapid subcellular processes. Nat. Biotechnol. **41**: 367–377. DOI: 10.1038/s41587-022-01471-3.
25. Wu, Y., Han, X., Su, Y., et al. (2021). Multiview confocal super-resolution microscopy. Nature **600**: 279–284. DOI: 10.1038/s41586-021-04110-0.
26. Zhang, B., Ouyang, C., Cui, P., et al. (2024). Deep learning for cross-region streamflow and flood forecasting at a global scale. The Innovation **5**: 100617. DOI: 10.1016/j.xinn.2024.100617.
27. Yuan, X. and Han, S. (2021). Single-pixel neutron imaging with artificial intelligence: Breaking the barrier in multi-parameter imaging, sensitivity, and spatial resolution. The Innovation **2**: 100100. DOI: 10.1016/j.xinn.2021.100100.
28. Ye, Z., Wang, N., Zhou, J., et al. (2024). Organic crystal structure prediction via coupled generative adversarial networks and graph convolutional networks. The Innovation **5**: 100562. DOI: 10.1016/j.xinn.2023.100562.
29. Li, S. and Xing, J. (2024). DeepSAT4D: Deep learning empowers four-dimensional atmospheric chemical concentration and emission retrieval from satellite. The Innovation Geoscience **2**: 100061–100011. DOI: 10.59717/j.xinn-geo.2024.100061.
30. Wang, Z., Zhang, J., Hua, P., et al. (2023). Filling in missing pieces in the co-development of artificial intelligence and environmental science. The Innovation Geoscience **1**: 100007–100015. DOI: 10.59717/j.xinn-geo.2023.100007.
31. Ma, H., Jiao, Y., Guo, W., et al. (2024). Machine learning predicts atomistic structures of multielement solid surfaces for heterogeneous catalysts in variable environments. The Innovation **5**: 100571. DOI: 10.1016/j.xinn.2024.100571.
32. Xun, D., Wang, R., Zhang, X., et al. (2024). Microsnoop: A generalist tool for microscopy image representation. The Innovation **5**: 100541. DOI: 10.1016/j.xinn.2023.100541.
33. Zhu, R., Zhang, F., Yan, J., et al. (2023). A sustainable solar city: From utopia to reality facilitated by GIScience. The Innovation Geoscience **1**: 100006–100013. DOI: 10.59717/j.xinn-geo.2023.100006.
34. Luo, L., Zong, X., Shao, J., et al. (2023). LiDARchaeology: A revolutionary approach to archaeological prospection in forested areas. The Innovation Geoscience **1**: 100017. DOI: 10.59717/j.xinn-geo.2023.100017.
35. Lü, G., Yue, S., Yu, Z., et al. (2023). Ubiquitous geographic information for building digital twins of geographic environments. The Innovation Geoscience **1**: 100023–100022. DOI: 10.59717/j.xinn-geo.2023.100023.
36. Gomariz, A., Portenier, T., Helbling, P.M., et al. (2021). Modality attention and sampling enables deep learning with heterogeneous marker combinations in fluorescence microscopy. Nat. Mach. Intell. **3**: 799–811. DOI: 10.1038/s42256-021-00379-y.
37. Ziatdinov, M., Ghosh, A., Wong, C.Y., et al. (2022). AtomAI framework for deep learning analysis of image and spectroscopy data in electron and scanning probe microscopy. Nat. Mach. Intell. **4**: 1101–1112. DOI: 10.1038/s42256-022-00555-8.
38. Kench, S. and Cooper, S.J. (2021). Generating three-dimensional structures from a two-dimensional slice with generative adversarial network-based dimensionality expansion. Nat. Mach. Intell. **3**: 299–305. DOI: 10.1038/s42256-021-00322-1.
39. Ledig, C., Theis, L., Huszár, F., et al. (2017). Photo-realistic single image super-resolution using a generative adversarial network. In 2017 IEEE Conference on Computer Vision and Pattern Recognition (CVPR). DOI: 10.1109/CVPR.2017.19.
40. Jiang, K., Wang, Z., Yi, P., et al. (2019). Edge-enhanced GAN for remote sensing image superresolution. IEEE Transactions on Geoscience and Remote Sensing **57**: 5799–5812. DOI: 10.1109/TGRS.2019.2902431.
41. Zhang, W., Liu, Y., Dong, C., et al. (2019). RankSRGAN: Generative adversarial networks with ranker for image super-resolution. In Proceedings of the IEEE/CVF International Conference on Computer Vision. DOI: 10.1109/ICCV.2019.00319.
42. Jiang, K., Wang, Z., Yi, P., et al. (2020). Hierarchical dense recursive network for image super-resolution. Pattern Recog. **107**: 107475. DOI: 10.1016/j.patcog.2020.107475.
43. Xiao, Y., Su, X., Yuan, Q., et al. (2022). Satellite video super-resolution via multiscale deformable convolution alignment and temporal grouping projection. IEEE T. Geoscience and Remote Sensing **60**: 1–19. DOI: 10.1109/TGRS.2021.3107352.
44. Hu, M., Jiang, K., Wang, Z., et al. (2023). CycMuNet+: Cycle-projected mutual learning for spatial-temporal video super-resolution. IEEE T. Pattern Analysis and Machine Intelligence **45**: 13376–13392. DOI: 10.1109/TPAMI.2023.3293522.
45. Xiao, Y., Yuan, Q., Jiang, K., et al. (2023). From degrade to upgrade: Learning a self-supervised degradation guided adaptive network for blind remote sensing image

super-resolution. Inform. Fusion 96: 297–311. DOI: 10.1016/j.inffus.2023.03.021.
46. Qiu, X., Li, M., Zhang, L., et al. (2019). Guided filter-based multi-focus image fusion through focus region detection. Signal Processing: Image Communication 72: 35–46. DOI: 10.1016/j.image.2018.12.004.
47. Dai, Y., Gieseke, F., Oehmcke, S., et al. (2021). Attentional feature fusion. In Proceedings of the IEEE/CVF Winter Conference on Applications of Computer Vision. DOI: 10.1109/WACV48630.2021.00360.
48. Li, W., Zhou, K., Qi, L., et al. (2022). Best-buddy gans for highly detailed image super-resolution. In Proceedings of the AAAI Conference on Artificial Intelligence. DOI: 10.1609/aaai.v36i2.20030.
49. Huynh-Thu, Q. and Ghanbari, M. (2008). Scope of validity of PSNR in image/video quality assessment. Electron. Lett. 44: 800–801. DOI: 10.1049/el:20080522.
50. Zhang, R., Isola, P., Efros, A.A., et al. (2018). The unreasonable effectiveness of deep features as a perceptual metric. In Proceedings of the IEEE Conference on Computer Vision and Pattern Recognition. DOI: 10.1109/CVPR.2018.00068.
51. Heusel, M., Ramsauer, H., Unterthiner, T., et al. (2017). GANs trained by a two time-scale update rule converge to a local nash equilibrium. In Proceedings of the 31st International Conference on Neural Information Processing Systems. DOI: 10.5555/3295222.3295408.
52. Blau, Y., Mechrez, R., Timofte, R., et al. (2018). The 2018 PIRM Challenge on Perceptual Image Super-Resolution. In Proceedings of the European Conference on Computer Vision (ECCV) Workshops. DOI: 10.1007/978-3-030-11021-5_21.
53. Wang, X., Yu, K., Wu, S., et al. (2018). ESRGAN: Enhanced super-resolution generative adversarial networks. In Proceedings of the European Conference on Computer Vision (ECCV) Workshops. DOI: 10.1007/978-3-030-11021-5_5.
54. Prajapati, K., Chudasama, V., Patel, H., et al. (2020). Unsupervised single image super-resolution network (USISResNet) for real-world data using generative adversarial network. In Proceedings of the IEEE/CVF Conference on Computer Vision and Pattern Recognition Workshops. DOI: 10.1109/CVPRW50498.2020.00240.
55. Prajapati, K., Chudasama, V., Patel, H., et al. (2021). Direct unsupervised super-resolution using generative adversarial network (DUS-GAN) for real-world data. IEEE T. Image Process. 30: 8251–8264. DOI: 10.1109/TIP.2021.3113783.
56. Marr, D. and Hildreth, E. (1980). Theory of Edge Detection. P. Roy. Society B-Biol. Sci. 207: 187–217. DOI: 10.1098/rspb.1980.0020.
57. Paris, S., Hasinoff, S.W., and Kautz, J. (2011). Local Laplacian filters: Edge-aware image processing with a Laplacian pyramid. In SIGGRAPH '11: Special Interest Group on Computer Graphics and Interactive Techniques Conference. DOI: 10.1145/1964921.1964963.
58. Kong, H., Akakin, H.C., and Sarma, S.E. (2013). A generalized laplacian of gaussian filter for blob detection and its applications. IEEE T. Cybernetics 43: 1719–1733. DOI: 10.1109/TSMCB.2012.2228639.
59. Jin, D., Chen, Y., Lu, Y., et al. (2021). Neutralizing the impact of atmospheric turbulence on complex scene imaging via deep learning. Nat. Mach. Intell. 3: 876–884. DOI: 10.1038/s42256-021-00392-1.
60. Bradley, R.A. and Terry, M.E. (1952). Rank analysis of incomplete block designs: I. The method of paired comparisons. Biometrika 39: 324–345. DOI: 10.2307/2334029.
61. Maritz, M.G. and Schoeman, J. (2022). Programmable aperture using a digital micromirror device for in-line holographic microscopy. IEEE J. Quantum Elect. 58: 1–8. DOI: 10.1109/JQE.2022.3190501.
62. Yang, J., Zhang, Z., and Cheng, Q. (2022). Resolution enhancement in micro-XRF using image restoration techniques. J. Anal. Atom. Spectrom. 37: 750–758. DOI: 10.1039/D1JA00425E.
63. Shi, Q., Lai, Y., Guo, H., et al. (2021). Fluid inclusion and C-O isotopic constrains on the origin and evolution of ore-forming fluids of the Badaguan Cu-Mo deposit, Inner Mongolia. Ore Geol. Rev. 136: 104267. DOI: 10.1016/j.oregeorev.2021.104267.

FUNDING AND ACKNOWLEDGMENTS

This project has received funding from the National Natural Science Foundation of China (62271016, 42192502), the Beijing Natural Science Foundation (4222007), the Shenzhen Natural Science Foundation (6023210102K), the Fundamental Research Funds for the Central Universities and the DDE-IUGS Big Science Program. The funders had no role in study design, data collection and analysis, decision to publish, or preparation of the manuscript.

AUTHOR CONTRIBUTIONS

H.S., X.X., and X.B. conceptualized the research, designed the methodology and wrote the paper. H.S., X.X., Q.S., and D.Y. performed the experiments and created the dataset. H.S., J.C. and D.J. developed the software. X.B., Y.L. and Y.L. supervised the research. All authors contributed to and approved the manuscript.

DECLARATION OF INTERESTS

The authors declare no competing interests.

DATA AND CODE AVAILABILITY

Data supporting the findings of this work and code used in this paper including the trained OIGAN model are available at https://github.com/a-Fomalhaut-a/OIGAN

SUPPLEMENTAL INFORMATION

It can be found online at https://doi.org/10.59717/j.xinn-geo.2024.100083

LEAD CONTACT WEBSITE

https://xzbai.buaa.edu.cn/